








## ARTICLE

<https://doi.org/10.1038/s42004-019-0232-2>

OPEN

# Bifurcation of self-assembly pathways to sheet or cage controlled by kinetic template effect

Leonardo Hayato Foianesi-Takeshige <sup>1</sup>, Satoshi Takahashi <sup>1</sup>, Tomoki Tateishi <sup>1</sup>, Ryosuke Sekine<sup>2</sup>, Atsushi Okazawa <sup>1</sup>, Wenchao Zhu<sup>2</sup>, Tatsuo Kojima <sup>1</sup>, Koji Harano<sup>2</sup>, Eiichi Nakamura<sup>2</sup>, Hirofumi Sato <sup>3,4</sup> & Shuichi Hiraoka <sup>1\*</sup>

The template effect is a key feature to control the arrangement of building blocks in assemblies, but its kinetic nature remains elusive compared to the thermodynamic aspects, with the exception of very simple reactions. Here we report a kinetic template effect in a self-assembled cage composed of flexible ditopic ligands and Pd(II) ions. Without template anion, a micrometer-sized sheet is kinetically trapped (off-pathway), which is converted into the thermodynamically most stable cage by the template anion. When the template anion is present from the start, the cage is selectively produced by the preferential cyclization of a dinuclear intermediate (on-pathway). Quantitative and numerical analyses of the self-assembly of the cage on the on-pathway revealed that the accelerating effect of the template is stronger for the early stage reactions of the self-assembly than for the final cage formation step itself, indicating the kinetic template effect.

<sup>1</sup>Department of Basic Science, Graduate School of Arts and Sciences, The University of Tokyo, 3-8-1 Komaba, Meguro-ku, Tokyo 153-8902, Japan.

<sup>2</sup>Department of Chemistry, Graduate School of Science, The University of Tokyo, 7-3-1 Hongo, Bunkyo-ku, Tokyo 113-0033, Japan. <sup>3</sup>Department of Molecular Engineering, Kyoto University, Kyoto 615-8510, Japan. <sup>4</sup>Elements Strategy Initiative for Catalysts and Batteries, Kyoto University, Kyoto 615-8510, Japan. \*email: [chiraoka@mail.ecc.u-tokyo.ac.jp](mailto:chiraoka@mail.ecc.u-tokyo.ac.jp)

As seen in DNA-replication, the template effect<sup>1,2</sup> is a powerful strategy for efficient synthesis of assemblies whose building blocks are well arranged, such as macrocycles<sup>3–9</sup>, cages<sup>10,11</sup>, interlocked and knotted molecules<sup>12–27</sup>, and submicrometer-sized materials<sup>28–34</sup>. Basically, this effect makes the interconnection of the building blocks feasible by their pre-organization by binding to the template molecule(s). As a consequence, the template effect is effective in the synthesis of assemblies composed of conformationally flexible building blocks. When the building blocks are connected by irreversible bonds, once an undesired bond is formed, such intermediates can never lead to the desired structure. Thus, the template molecule biases the reaction towards the correct pathway by modulating the energy landscape so as to selectively decrease the energy barriers of proper bond connections under kinetic control<sup>2</sup>. In molecular self-assembly, where building blocks are connected by reversible bonds, the reaction is rather controlled by thermodynamics. Owing to the reversible nature of the chemical bonds between the building blocks, even when the building blocks are connected in an incorrect manner, the thermodynamically most stable structure is produced under thermodynamic control by correction of the interconnections. Therefore, the thermodynamic template effect plays a major role in most molecular self-assembly systems<sup>13,15,18</sup>. As the template molecule that stabilizes the final assembly would also stabilize the transition states and the intermediates produced along the correct self-assembly pathway(s), the importance of the kinetic template effect on molecular self-assembly has been implied but is not clearly understood.

Here we report a bifurcation of self-assembly pathways by a kinetic template that determines the product, a kinetically trapped micrometer-sized sheet structure or the thermodynamically most stable 1-nm-sized coordination cage. In the absence of the template molecule ( $\text{NO}_3^-$ ), the self-assembly of ditopic ligand **1** and Pd(II) source ( $[\text{PdPy}^*_4](\text{OTf})_2$ ,  $\text{Py}^*$  indicates 3-chloropyridine) leads to a metastable micrometer-sized sheet structure as a major product under kinetic control (Fig. 1). With the template, the

$(\text{NO}_3^-)@[\text{Pd}_2\mathbf{1}_4]^{4+}$  cage, where one  $\text{NO}_3^-$  anion is bound to the cavity of the cage, is produced in 79% yield through the on-pathway. Quantitative and numerical analyses of the self-assembly of the cage in the presence of the template anion revealed that the production of the intermediates for the cage is significantly accelerated by the template anion, which is also confirmed by the acceleration of the formation of a cyclic model structure in the presence of  $\text{NO}_3^-$  and the strong binding of the cyclic structure with  $\text{NO}_3^-$ . Besides the stabilization of the final cage by the encapsulation of  $\text{NO}_3^-$ , a kinetic template effect accelerates the formation of primitive intermediates for the cage by the template anion and contributes strongly to the bifurcation of the self-assembly pathways.

## Results

**Micrometer-sized sheet formation on the off-pathway.** The self-assembly of the helical  $[\text{Pd}_2\mathbf{1}_4]^{4+}$  cage was reported by Steel and McMoran<sup>35,36</sup>. Due to the high flexibility of the ditopic ligand **1**, the resulting cage can bind a variety of anionic species ( $\text{PF}_6^-$ ,  $\text{BF}_4^-$ ,  $\text{ClO}_4^-$ ,  $\text{ReO}_4^-$ , and  $\text{I}^-$ ) in its cavity, whose size can be changed by twisting the helix in an induced-fit manner. The order of the binding strength for anions is  $\text{ClO}_4^- > \text{BF}_4^- > \text{ReO}_4^- > \text{PF}_6^-$ , which suggests that smaller anions are more strongly bound in the cage with the exception that  $\text{ClO}_4^-$  (62.5 Å<sup>3</sup>) is a better guest than  $\text{BF}_4^-$  (49.3 Å<sup>3</sup>)<sup>36</sup>. The self-assembly of the cage from **1** and  $[\text{PdPy}^*_4](\text{OTf})_2$  in  $\text{CD}_3\text{NO}_2$  at 298 K was carried out to investigate the intermediates produced during the self-assembly by QASAP (quantitative analysis of self-assembly process)<sup>37–39</sup>. In our previous research on the self-assembly process of this cage from **1** and  $[\text{PdPy}^*_4](\text{BF}_4)_2$ , a 200-nm-sized sheet structure was transiently produced during the self-assembly and this sheet structure was finally converted to the  $(\text{BF}_4^-)@[\text{Pd}_2\mathbf{1}_4]^{4+}$  cage<sup>40</sup>. When the self-assembly of the cage was carried out using  $\text{OTf}^-$  as a counter anion and monitored by <sup>1</sup>H NMR spectroscopy (Fig. 2, Supplementary Fig. 1 and Supplementary

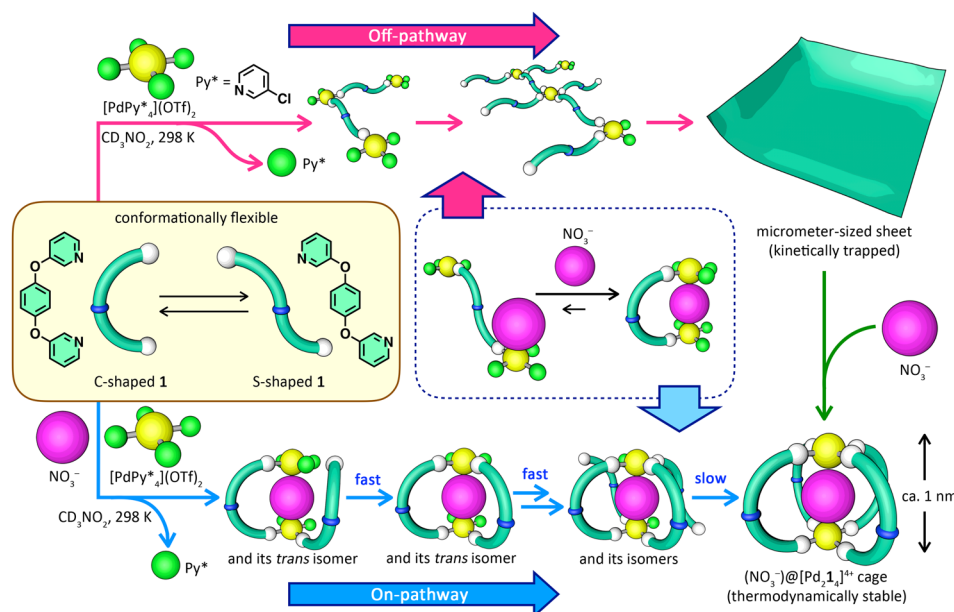


**Fig. 1** Summary of the self-assembly of the  $[\text{Pd}_2\mathbf{1}_4]^{4+}$  cage. A schematic representation of the bifurcation of pathways for the self-assembly of the  $(\text{NO}_3^-)@[\text{Pd}_2\mathbf{1}_4]^{4+}$  cage from ditopic ligand **1** and  $[\text{PdPy}^*_4](\text{OTf})_2$ . Due to the conformational flexibility of **1**, **1** adopts C- and S-shaped conformations in solution. In the absence of a good template ( $\text{NO}_3^-$ ), oligomerization is preferred from S-shaped ligands to lead to a kinetically trapped micrometer-sized sheet structure (off-pathway). The sheet can be converted to the thermodynamically stable  $[\text{Pd}_2\mathbf{1}_4]^{4+}$  cage by a good template,  $\text{NO}_3^-$ . The cage can be produced through the other pathway in the presence of  $\text{NO}_3^-$  (on-pathway), where the C-shaped conformation is induced by the template to form the  $(\text{NO}_3^-)@[\text{Pd}_2\mathbf{1}_4]^{4+}$  cyclic structure

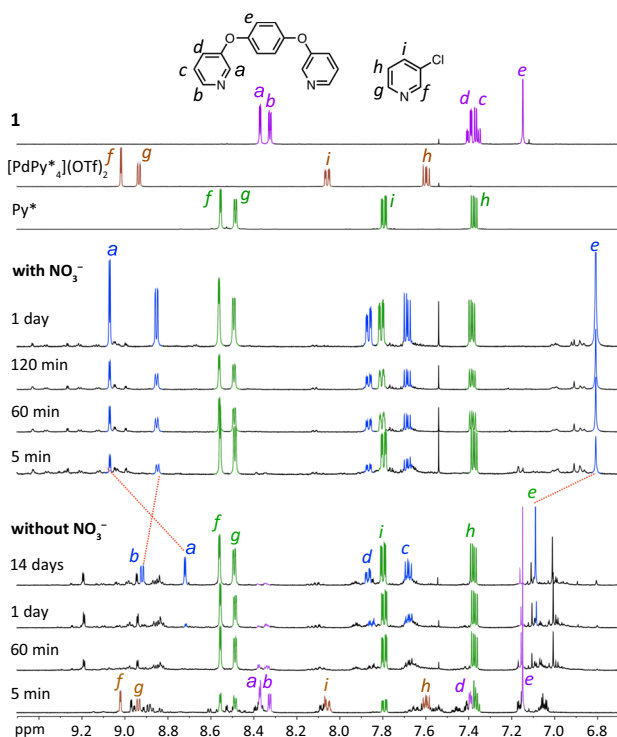


**Fig. 2** Monitoring of the self-assembly of the  $[\text{Pd}_2\mathbf{1}_4]^{4+}$  cage by  $^1\text{H}$  NMR spectroscopy.  $^1\text{H}$  NMR spectra (500 MHz,  $\text{CD}_3\text{NO}_2$ , 298 K) of the reaction mixture of the self-assembly of the  $[\text{Pd}_2\mathbf{1}_4]^{4+}$  cage from **1** and  $[\text{PdPy}^*_4](\text{OTf})_2$  in  $\text{CD}_3\text{NO}_2$  at 298 K with and without  $\text{NO}_3^-$ .  $[\mathbf{1}]_0 = 2.0 \text{ mM}$ ,  $[\text{Pd}]_0 = 1.0 \text{ mM}$ ,  $[\text{NO}_3^-]_0 = 2.0 \text{ mM}$

Tables 1–6), the cage formation was significantly retarded (Fig. 3a). The yield of the  $(\text{OTf}^-)@[\text{Pd}_2\mathbf{1}_4]^{4+}$  cage at 1 day is only 6.3%, while that of the  $(\text{BF}_4^-)@[\text{Pd}_2\mathbf{1}_4]^{4+}$  cage at 1 day is 68.3%<sup>40</sup>. The encapsulation of one  $\text{OTf}^-$  anion in the cage was confirmed by  $^{19}\text{F}$  NMR and  $^{19}\text{F}$  DOSY measurements (Supplementary Fig. 2 and Supplementary Table 7). This result indicates that the counter anion largely affects the self-assembly process. STEM measurements of a reaction mixture after the convergence of the self-assembly indicate that a sheet structure was also produced in the self-assembly from **1** and  $[\text{PdPy}^*_4](\text{OTf})_2$  (Fig. 4a–e). However, the size of the sheet (over  $100 \mu\text{m}$ ) is much larger than that produced from **1** and  $[\text{PdPy}^*_4](\text{BF}_4)_2$ . Several dark areas can be seen in the STEM images, which would be formed by tangling of the sheet, suggesting that this sheet is a flexible, soft material. The same tangled sheet structures were observed by AFM measurements of a dried sample of the reaction mixture (Fig. 4f, g). Apart from the tangled parts (Fig. 4i), this sheet is relatively smooth and a step with a gap of 4.44 nm was found (Fig. 4h).

The formation of the sheet was not prevented even in the case where the self-assembly was carried out at  $70^\circ\text{C}$  and the yield of the cage was not improved by heating (Supplementary Figs. 3 and 4), indicating that the sheet produced from **1** and  $[\text{PdPy}^*_4](\text{OTf})_2$  is more stable than the sheet produced from **1** and  $[\text{PdPy}^*_4](\text{BF}_4)_2$ <sup>40</sup> and that most of the  $(\text{OTf}^-)@[\text{Pd}_2\mathbf{1}_4]^{4+}$  cages produced under this condition (35%) would not be derived from the sheet. Indeed, when the self-assembly was conducted with  $\text{BARF}^-$  (tetrakis[3,5-bis(trifluoromethyl)phenyl]borate), which is too large to be encapsulated in the  $[\text{Pd}_2\mathbf{1}_4]^{4+}$  cage, the  $[\text{Pd}_2\mathbf{1}_4]^{4+}$  cage was produced in 17% yield without a template anion (Supplementary Figs. 5 and 6).

As the sheet structure is kinetically trapped, the self-assembly using  $\text{OTf}^-$  anion tends to promote the growth of the sheet structure under kinetic control, suggesting that  $\text{OTf}^-$  is not a

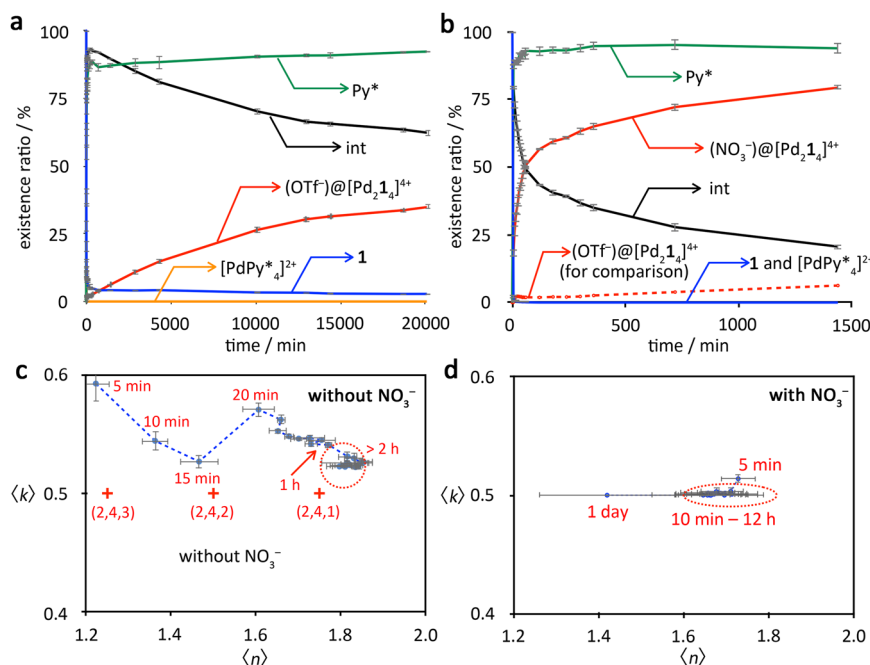


**Fig. 3** QASAP data for the self-assembly of the  $(\text{X}^-)@[\text{Pd}_2\mathbf{1}_4]^{4+}$  cage. The self-assembly was conducted from **1** and  $[\text{PdPy}^*_4](\text{OTf})_2$  in  $\text{CD}_3\text{NO}_2$  at 298 K with and without  $\text{NO}_3^-$ . **a** Existence ratios of the substrates and the products for the self-assembly of the cage without  $\text{NO}_3^-$ .  $[\mathbf{1}]_0 = 2.0 \text{ mM}$ ,  $[\text{Pd}]_0 = 1.0 \text{ mM}$ . **b** Existence ratios of the substrates and the products for the self-assembly of the cage with  $\text{NO}_3^-$ .  $[\mathbf{1}]_0 = 2.0 \text{ mM}$ ,  $[\text{Pd}]_0 = 1.0 \text{ mM}$ ,  $[\text{NO}_3^-]_0 = 2.0 \text{ mM}$ . **c** An  $n$ - $k$  plot for the self-assembly of the cage without  $\text{NO}_3^-$ . **d** An  $n$ - $k$  plot for the self-assembly of the cage with  $\text{NO}_3^-$ . Error bars indicate the standard errors of the means of the existence ratios (**a** and **b**) and the  $\langle n \rangle$ ,  $\langle k \rangle$  values (**c** and **d**). The  $(n, k)$  value for  $\text{Pd}_6\mathbf{1}_6\text{Py}_6^*$  indicates as  $(a, b, c)$

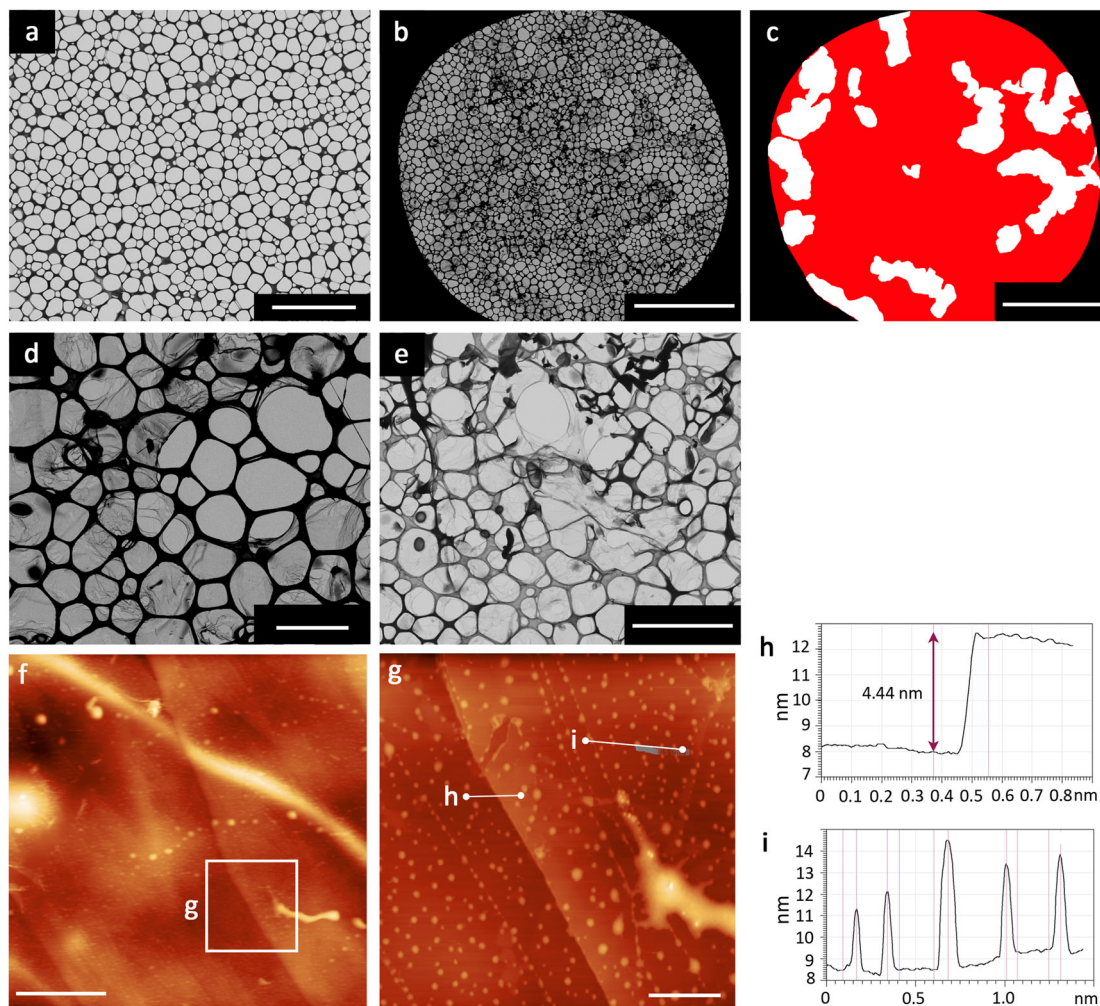


**Fig. 4** Characterization of the sheet structure. The sheet was produced in the self-assembly from **1** and  $[\text{PdPy}^*_4](\text{OTf})_2$  with  $n\text{-Bu}_4\text{NOTf}$  in  $\text{CD}_3\text{NO}_2$  at 298 K. **a–e** STEM on a TEM microgrid and **f–i** AFM on a graphene substrate (dried sample of the reaction mixture). **a** An empty TEM microgrid. The scale bar indicates 20  $\mu\text{m}$ . **b** Whole image on a TEM microgrid. The white area corresponds to the background grid and the dark area corresponds to the very thin sheet-type structure. The scale bar indicates 40  $\mu\text{m}$ . **c** The sheet structure in **b** is shown in red, while white areas indicate bare TEM microgrid. The scale bar indicates 40  $\mu\text{m}$ . **d, e** Magnified images of the very thin sheet-type structure. The scale bars in **d** and **e** indicate 5 and 10  $\mu\text{m}$ , respectively. **f** A  $20 \times 20 \mu\text{m}^2$  AFM image. The scale bar indicates 5  $\mu\text{m}$ . A  $5 \times 5 \mu\text{m}^2$  white square indicates the scanning area for **g**. **g** Magnified  $5 \times 5 \mu\text{m}^2$  image of **f**. The scale bar indicates 1  $\mu\text{m}$ . The white lines in **g** indicate the extracted profile to measure the height. **h** and **i** Height profiles. **h** Crosses over the difference in levels (4.44 nm) where a sheet is on top of another sheet. **i** Crosses over five lumps

good guest for the  $[\text{Pd}_2\text{I}_4]^{4+}$  cage. As expected, competition experiments indicate that smaller  $\text{BF}_4^-$  is a stronger guest than  $\text{OTf}^-$  (90.5  $\text{\AA}^3$ ) for the cage (Supplementary Figs. 7–9 and Supplementary Table 8). To check the ability of counter anions to convert the sheet into the cage,  $n\text{-Bu}_4\text{NX}$  (X:  $\text{ClO}_4^-$ ,  $\text{BF}_4^-$ , or  $\text{PF}_6^-$ ) was added after the formation of the sheet prepared from **1** and  $[\text{PdPy}^*_4](\text{OTf})_2$  (Supplementary Figs. 10–16 and Supplementary Tables 9–11). The rate of the conversion of the sheet to the cage became faster by the addition of smaller guests, indicating that the conversion ability seems to correlate to the size of the anions.

**The cage formation on the on-pathway.** In the competition experiments of various anions, it was found that  $\text{NO}_3^-$  (42.3  $\text{\AA}^3$ ) is more strongly bound to the cage than  $\text{ClO}_4^-$  (Supplementary Fig. 17). Therefore, the addition of  $n\text{-Bu}_4\text{NNO}_3$  considerably accelerated the conversion of the sheet to the cage compared with  $n\text{-Bu}_4\text{NClO}_4$  or  $n\text{-Bu}_4\text{NBF}_4$  (Supplementary Fig. 16 and Supplementary Table 12). We then carried out the self-assembly from **1**

and  $[\text{PdPy}^*_4](\text{OTf})_2$  in the presence of  $n\text{-Bu}_4\text{NNO}_3$  to prevent the formation of the sheet during the self-assembly (Fig. 2 and Supplementary Tables 13–17). The  $^1\text{H}$  NMR signals of the  $(\text{NO}_3^-)@[\text{Pd}_2\text{I}_4]^{4+}$  cage were clearly observed even at 5 min and the self-assembly reaction almost converged in 1 day to produce the cage in 79% yield (Fig. 3b), indicating that the cage formation is dramatically accelerated by  $\text{NO}_3^-$ . The  $\text{H}^a$  signal of the  $(\text{NO}_3^-)@[\text{Pd}_2\text{I}_4]^{4+}$  cage was largely shifted downfield by 0.36 ppm as compared with that of the  $(\text{OTf}^-)@[\text{Pd}_2\text{I}_4]^{4+}$  cage (Fig. 2), which suggests that  $\text{NO}_3^-$  was strongly bound to the cavity of the cage.

**Crystal structure of the  $(\text{NO}_3^-)@[\text{Pd}_2\text{I}_4]^{4+}$  cage.** The structure of the  $(\text{NO}_3^-)@[\text{Pd}_2\text{I}_4]^{4+}$  cage was revealed by single-crystal X-ray analysis (Fig. 5, Supplementary Figs. 18 and 19, and Supplementary Tables 18 and 19). Single crystals of the  $(\text{NO}_3^-)@[\text{Pd}_2\text{I}_4]^{4+}$  cage were obtained from a solution of the cage in  $\text{CH}_3\text{NO}_2$  by slow diffusion of  $i\text{-Pr}_2\text{O}$  at 298 K for 10 days. The cage was strongly twisted with a twist angle of  $84.6^\circ$  accompanied by a short Pd...Pd distance of 7.167  $\text{\AA}$ , which are similar to those

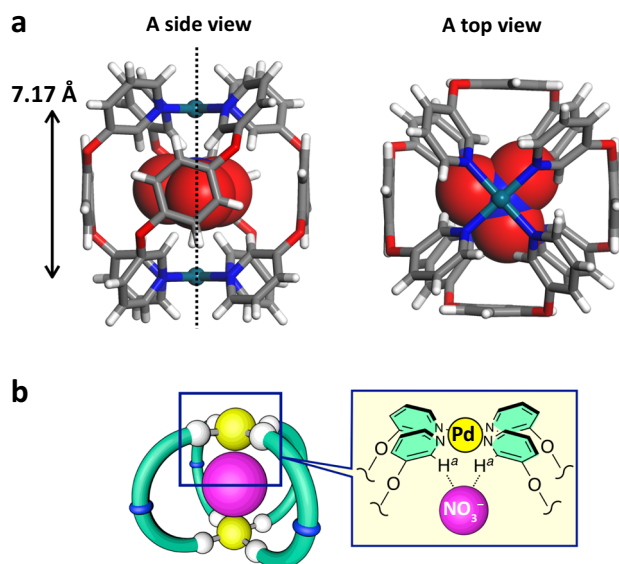


**Fig. 5** Crystal structure of  $(\text{NO}_3^-)@[\text{Pd}_2\text{I}_4]^{4+}$ . **a** Top and side views of the  $(\text{NO}_3^-)@[\text{Pd}_2\text{I}_4]^{4+}$  cage. Color labels: turquoise, Pd; gray, C; blue, N; red, O; white, H. The dotted black line in the side view indicates the helix axis. **b** Schematic indication of the hydrogen bonding interaction of the pyridyl hydrogen atoms ( $\text{H}^a$ ) and the  $\text{NO}_3^-$  anion encapsulated in the cage

of the  $(\text{I}^-)@[\text{Pd}_2\text{I}_4]^{4+}$  cage ( $84.8^\circ$ ,  $7.442 \text{ \AA}$ )<sup>36</sup>. The  $\text{NO}_3^-$  anion in the cage was disordered between two sites with each occupancy of 50% at the Wyckoff position of  $4a$  on the  $C_2$  axis, lying on a plane perpendicular to the helix axis of the cage. The shortest distance between the  $\text{H}^a$  hydrogen and the oxygen atoms of the  $\text{NO}_3^-$  is  $2.33 \text{ \AA}$ , which is shorter than the sum of the van der Waals radii of hydrogen and oxygen atoms, indicating that the  $\text{CH}\cdots\text{O}$  hydrogen bond stabilizes the inclusion complex<sup>41–45</sup>. Similar hydrogen bonds are found in the crystal structure of  $(\text{ClO}_4^-)@[\text{Pd}_2\text{I}_4]^{4+}$ <sup>36</sup>, suggesting that the stronger binding affinity of  $\text{ClO}_4^-$  to the cage than that of  $\text{BF}_4^-$ , which is smaller than  $\text{ClO}_4^-$ , is due to the stronger hydrogen bonds between  $\text{ClO}_4^-$  and the cage. The average distance between the oxygen atoms in the  $\text{NO}_3^-$  and the benzene ring of the ligand **1** is  $3.72 \text{ \AA}$ . When the Pd–Pd distance decreases by increasing the twist angle of the cage, the electron-rich aromatic walls in the cage are slightly moved further from each other, reducing the electrostatic repulsion between the walls and the anion encapsulated in the cage. This would be the reason why the  $[\text{Pd}_2\text{I}_4]^{4+}$  cage prefers smaller anions.

**Investigation of the self-assembly process of the cage.** The self-assembly process of the cage was investigated by the  $n$ – $k$  analysis<sup>37–39</sup>. The  $n$  value indicates the average number of the Pd(II) ions bound to a ditopic ligand **1** in a species  $[\text{Pd}_a\text{I}_b\text{Py}_c]^{2a+}$  ( $n = (4a - c)/b$ ), while the  $k$  value indicates the ratio of the Pd(II) ions to the ditopic ligands ( $k = a/b$ ). The experimentally obtained  $(n, k)$  values, which are indicated as  $(\langle n \rangle, \langle k \rangle)$ , are the  $(n, k)$  values of the average composition of all the intermediates  $[\text{Pd}_{(a)}\text{I}_{(b)}\text{Py}_{(c)}]^{2a+}$ , which can be determined by the quantification of all the substrates (**1** and  $[\text{PdPy}_4]^{2+}$ ) and the products ( $(\text{NO}_3^-)@[\text{Pd}_2\text{I}_4]^{4+}$  and  $\text{Py}^*$ ). The change in the  $(\langle n \rangle, \langle k \rangle)$  value with time suggests the type of occurring reactions and the mainly produced intermediates during the self-assembly.

In the absence of  $\text{NO}_3^-$  (off-pathway), the  $\langle n \rangle$  value largely and monotonically increased with time, while the  $\langle k \rangle$  value fluctuated around  $0.55$  (Fig. 3c). As most of the substrates were

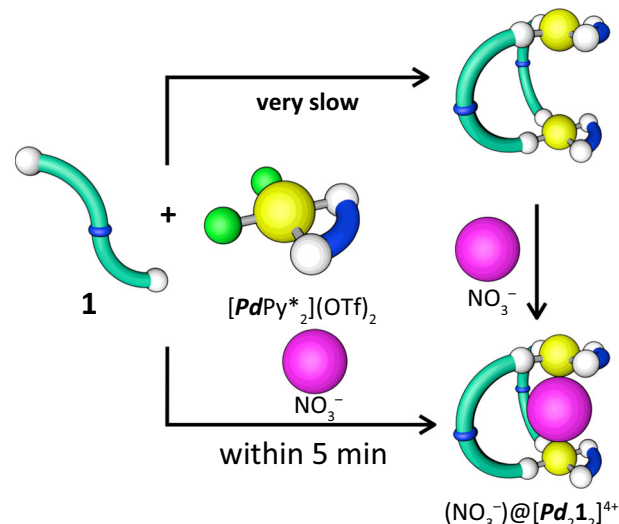


**Fig. 6** The template effect of  $\text{NO}_3^-$  in the self-assembly of the  $[\text{Pd}_2\text{I}_2]^{4+}$  model. **Pd** indicates Pd(*N,N,N',N'*-tetramethylethylenediamine)

consumed within 30 min, the increase in the  $\langle n \rangle$  value after 30 min suggests the growth of the oligomers and/or cross-linking by intra- and/or intermolecular ligand exchanges to release  $\text{Py}^*$ , which causes a decrease in the  $\langle c \rangle$  value. The  $(\langle n \rangle, \langle k \rangle)$  value reached  $(1.82, 0.52)$  at 2 h and stayed around  $(1.83, 0.52)$  until the end of the self-assembly. Considering that the largest  $n$  value among possible intermediates with the  $k$  value of  $0.5$  on the on-pathway is  $1.75$  for  $[\text{Pd}_2\text{I}_4\text{Py}^*]^{4+}$ , the experimental  $\langle n \rangle$  value of  $1.83$ , which is higher than  $1.75$ , suggests the production of intermediates larger than the cage<sup>40</sup>, which is consistent with the observation of the sheet structure.

In the self-assembly reaction carried out in the presence of  $\text{NO}_3^-$  (on-pathway), the  $(\langle n \rangle, \langle k \rangle)$  value stayed around  $(1.67, 0.50)$  from 10 min to 12 h (Fig. 3d), while the cage was drastically yielded to up to 72%, after which the self-assembly almost reached convergence. The steady  $(\langle n \rangle, \langle k \rangle)$  value during the production of a large amount of the cage indicates that dominant intermediates have  $(n, k)$  values close to the observed  $(\langle n \rangle, \langle k \rangle)$ <sup>46</sup>. The  $(\langle n \rangle, \langle k \rangle)$  value of  $(1.67, 0.50)$  is situated in between the  $(n, k)$  values of  $[\text{Pd}_2\text{I}_4\text{Py}_2]^{4+}$  ( $1.5, 0.5$ ) and of  $[\text{Pd}_2\text{I}_4\text{Py}^*]^{4+}$  ( $1.75, 0.5$ ), which correspond to the final precursors of the cage on the on-pathway. This result indicates that these two partial cage structures are mainly produced as intermediates from an early stage of the self-assembly and then the intramolecular cross-linking occurs as the rate-determining step. This would be because the rigidity of  $[\text{Pd}_2\text{I}_4\text{Py}_2]^{4+}$  and  $[\text{Pd}_2\text{I}_4\text{Py}^*]^{4+}$  hinders the formation of the intermediates and transition states with a five-coordinate Pd(II) center that should be formed during intramolecular ligand exchanges on Pd(II) centers<sup>47,48</sup>. As a consequence, the template  $\text{NO}_3^-$  anion much contributes to the early stage of the self-assembly of the  $(\text{NO}_3^-)@[\text{Pd}_2\text{I}_4]^{4+}$  cage; the  $\text{NO}_3^-$  anion kinetically affects the self-assembly to a great extent.

To demonstrate the strong binding between primitive intermediates and the  $\text{NO}_3^-$  anion on the on-pathway, the complexation of a model  $[\text{Pd}_2\text{I}_2]^{4+}$  macrocycle (**Pd** indicates Pd(*N,N,N',N'*-tetramethylethylenediamine)) with the  $\text{NO}_3^-$  anion was tested (Fig. 6). Upon the addition of *n*-Bu<sub>4</sub>NNO<sub>3</sub> in a  $\text{CD}_3\text{NO}_2$  solution of the  $[\text{Pd}_2\text{I}_2]^{4+}$  macrocycle, the  $\text{H}^a$  signal was as largely shifted downfield ( $0.36 \text{ ppm}$ ) as was observed in the  $(\text{NO}_3^-)@[\text{Pd}_2\text{I}_4]^{4+}$  cage (Supplementary Fig. 20). This result indicates that  $\text{NO}_3^-$  can be strongly bound to the cyclic structure,

which suggests that the intramolecular cyclization of  $(\text{NO}_3^-)@[\text{Pd}_2\text{I}_2\text{Py}^*]^{4+}$  to the  $(\text{NO}_3^-)@[\text{Pd}_2\text{I}_2\text{Py}^*]^{4+}$  macrocycle should be promoted by the kinetic template effect of the  $\text{NO}_3^-$  anion. Indeed, the formation of the  $[\text{Pd}_2\text{I}_2]^{4+}$  macrocycle completed within 5 min in the presence of  $\text{NO}_3^-$ , while the yield of the macrocycle without  $\text{NO}_3^-$  at 5 min is negligible (Supplementary Fig. 20). The competition experiment for  $\text{NO}_3^-$  between the  $[\text{Pd}_2\text{I}_4]^{4+}$  cage and the  $[\text{Pd}_2\text{I}_2]^{4+}$  macrocycle indicates that the cage is a stronger host for  $\text{NO}_3^-$  than the macrocycle (Supplementary Fig. 21), which is because the cage is structurally more organized than the macrocycle. Therefore,  $\text{NO}_3^-$  anion has a bilateral template effect on the on-pathway: (i) the kinetic template effect that accelerates intramolecular cyclization of the intermediates on the on-pathway, and (ii) the thermodynamic template effect that stabilizes the final cage.

**Numerical analysis of the self-assembly process of the cage.** To investigate the self-assembly process of the  $(\text{NO}_3^-)@[\text{Pd}_2\text{I}_4]^{4+}$  cage on the on-pathway in more detail, numerical analysis (NASAP: numerical analysis of self-assembly process<sup>49–51</sup>) was carried out based on the experimental data. The numerical analysis enables us to learn about the intermediates that cannot be deduced by QASAP. As the behavior of the self-assembly of the  $(\text{NO}_3^-)@[\text{Pd}_2\text{I}_4]^{4+}$  cage is similar to that of the cage self-assembly from the rigid ditopic ligand, NASAP for the present cage was carried out in a similar way to the rigid cage system<sup>50</sup>. A minimum reaction network considering substrates, products, and 25 intermediates composed of no more components than in the cage ( $[\text{Pd}_a\text{I}_b\text{Py}^*]^{2a+}$  ( $a \leq 2$ ,  $b \leq 4$ )) was prepared. All the reactions in the network (68 in total) are classified into the five types shown in Fig. 7a. As a result of NASAP, we found several solutions with

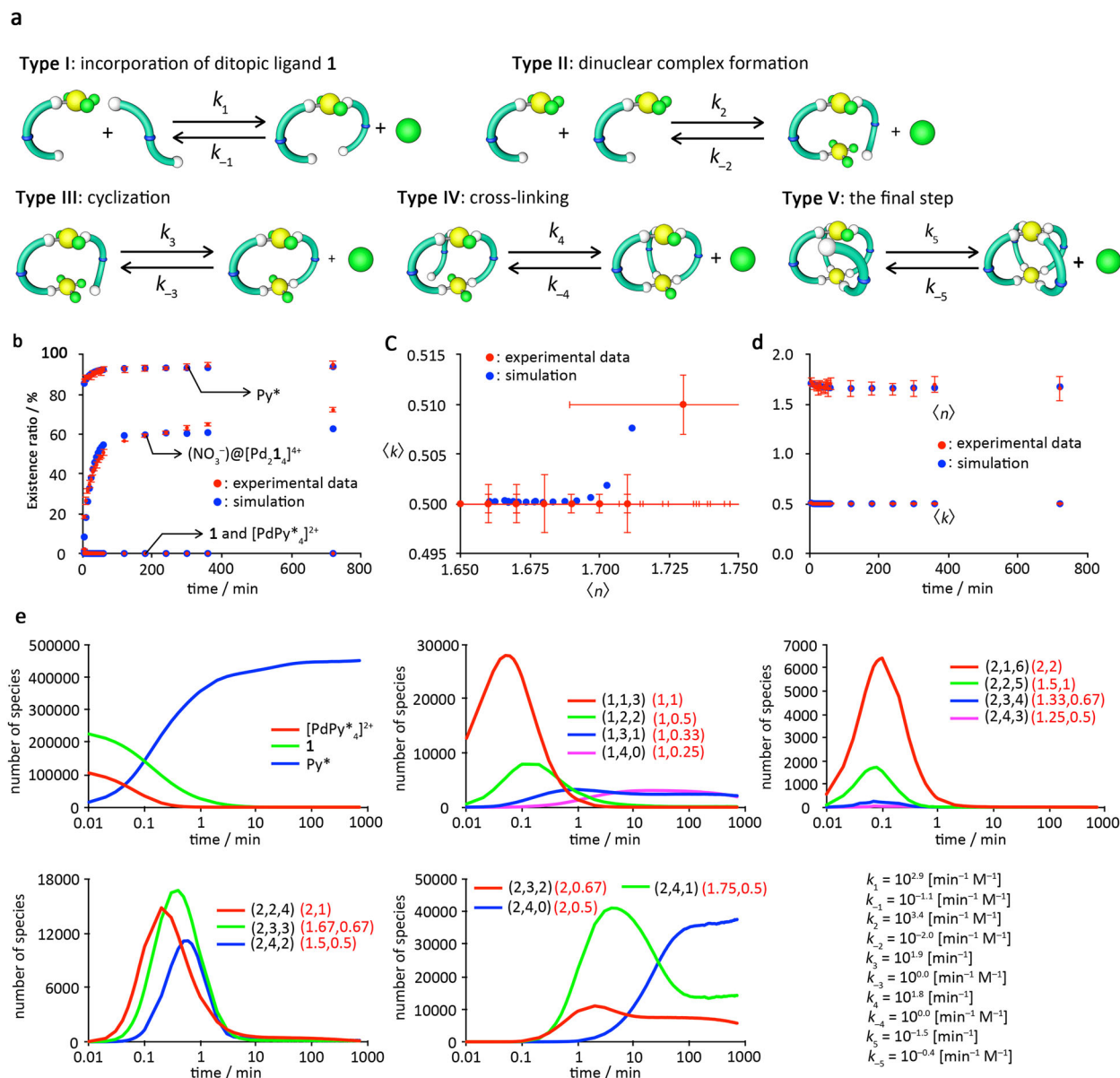


**Fig. 7** NASAP data for the self-assembly of the  $[\text{Pd}_2\text{I}_4]^{4+}$  cage. The self-assembly from 1 and  $[\text{PdPy}^*_4](\text{OTf})_2$  in  $\text{CD}_3\text{NO}_2$  at 298 K with  $\text{NO}_3^-$  was simulated. **a** The five reaction types in the network model of the self-assembly. Typical examples are shown in each type. The template anions encapsulated are omitted for clarity. A full network is shown in Supplementary Fig. 22. **b** Existence ratios of the substrates and the products with time. **c** Experimental and simulated  $n$ - $k$  plots. **d** Experimental and simulated  $\langle n \rangle$ ,  $\langle k \rangle$  values with time. **e** Time variation of major species by simulation and a list of the rate constants found by NASAP. (a, b, c) indicates  $[\text{Pd}_a\text{I}_b\text{Py}^*]^{2a+}$ . The (n, k) value of  $[\text{Pd}_a\text{I}_b\text{Py}^*]^{2a+}$  is also indicated in red

different sets of rate constants reproducing well the experimental results of time-dependent existence ratios of the substrates and the products in addition to the  $\langle n \rangle$ ,  $\langle k \rangle$  values (Fig. 7b–d). However, all the solutions have similar features as follows:

- (1) Very similar  $k_1 = 10^{2.9} \text{ min}^{-1} \text{ M}^{-1}$ ,  $k_2 = 10^{3.4} \text{ min}^{-1} \text{ M}^{-1}$ ,  $k_5 = 10^{-1.5} \text{ min}^{-1}$ , and  $k_{-5} = 10^{-0.4} \text{ min}^{-1} \text{ M}^{-1}$  values were obtained.
- (2) As the rates of backward reactions except in the final step ( $k_{-5}$ ) are significantly smaller than those of the corresponding forward reactions, these rate constants ( $k_{-1}$ ,  $k_{-2}$ ,  $k_{-3}$ , and  $k_{-4}$ ) do not much affect the self-assembly, which is confirmed by the result that the number of backward reactions is negligibly small in all the reaction steps except for the final stage. This result indicates that even though the Pd(II)–N bond formation is reversible, the self-assembly proceeds in an irreversible manner, which would be because the template anion navigates the self-assembly along the correct pathways.

According to the experimental result showing the considerably quick formation of  $(\text{NO}_3^-)@[\text{Pd}_2\mathbf{1}_2]^{4+}$  (Fig. 6), the large  $k_3$  value can be estimated. Based on this, a suitable set of rate constants in the cyclization ( $k_3$  and  $k_{-3}$ ) and cross-linking ( $k_4$  and  $k_{-4}$ ) steps were chosen from the data sets that reproduce the experimental data. One of the typical results is shown in Fig. 7b–e.  $k_3$  ( $10^{1.9} \text{ min}^{-1}$ ) and  $k_4$  ( $10^{1.8} \text{ min}^{-1}$ ) are much larger than  $k_5$  ( $10^{-1.5} \text{ min}^{-1}$ ), which indicates that the intramolecular cross-linking in the early stage of the self-assembly is promoted by the kinetic template effect of  $\text{NO}_3^-$ . In the early stage of the self-assembly,  $[\text{Pd}_2\mathbf{1}\text{Py}^*_6]^{4+}$  is mainly produced (Fig. 7e). Then,  $[\text{Pd}_2\mathbf{1}_2\text{Py}^*_4]^{4+}$ ,  $[\text{Pd}_2\mathbf{1}_3\text{Py}^*_3]^{4+}$ , and  $[\text{Pd}_2\mathbf{1}_4\text{Py}^*_2]^{4+}$  are produced. Finally,  $[\text{Pd}_2\mathbf{1}_4\text{Py}^*]^{4+}$  becomes the dominant species, which is due to a small  $k_5$ .

**Kinetic template effect in the cage assembly.** According to the results mentioned above, the energy landscape of the self-assembly of the cage is schematically shown in Fig. 8. Whether the self-assembly proceeds towards the formation of the cage (on-pathway) or towards the sheet structure (off-pathway) is kinetically controlled by the difference between the energy barriers of the intra- and intermolecular reactions in the primitive dinuclear intermediates such as  $[\text{Pd}_2\mathbf{1}_2\text{Py}^*_5]^{4+}$ . Without  $\text{NO}_3^-$ , the energy barrier of the formation of the sheet ( $\Delta G_{\text{off}}^\ddagger$ ) is smaller than that of the  $(\text{OTf}^-)@[\text{Pd}_2\mathbf{1}_4]^{4+}$  cage ( $\Delta G_{\text{on}}^\ddagger$ ), which is mainly due to the preference of open structures with S-shaped ditopic ligands, so the metastable sheet structure is kinetically trapped through the off-pathway. In the presence of  $\text{NO}_3^-$ , this good template anion induces the C-shaped conformation in the dinuclear complexes, which decreases the energy barrier of the formation of the cage by preorganization to open the on-pathway ( $\Delta G_{\text{off}}^\ddagger > \Delta G_{\text{on}}^\ddagger$ ).

## Discussion

In the self-assembly from ditopic ligand **1** and  $[\text{PdPy}^*_4]^{2+}$ , the reaction pathway was largely affected by the counter anions. For the self-assembly with  $\text{OTf}^-$  anions (off-pathway), the very weak template effect of  $\text{OTf}^-$  caused the production of the kinetically trapped sheet structure larger than  $100 \mu\text{m}$ . In contrast, the presence of  $\text{NO}_3^-$  in the self-assembly afforded the thermodynamically most stable  $(\text{NO}_3^-)@[\text{Pd}_2\mathbf{1}_4]^{4+}$  cage, whose production was significantly accelerated by the kinetic template effect (on-pathway). QASAP for the cage formation elucidated that the  $\text{NO}_3^-$  anion promotes the reactions in the early stage of the self-assembly to a greater extent than those in the final step. This result is supported by the high binding affinity of a cyclic  $[\text{Pd}_2\mathbf{1}_2]^{4+}$  model complex for  $\text{NO}_3^-$  and the acceleration of the

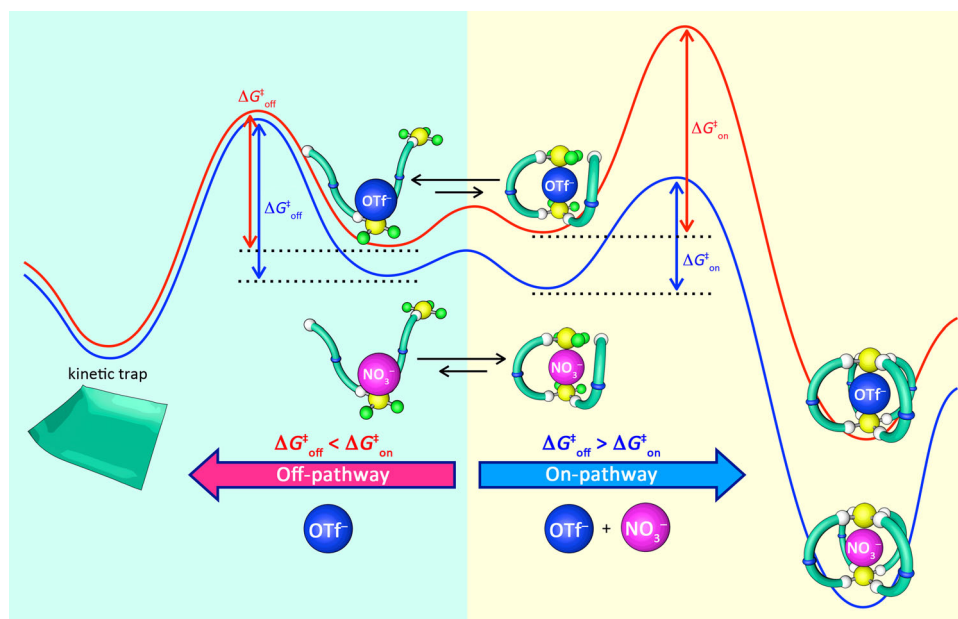


**Fig. 8** A simplified energy landscape of the self-assembly of the cage. It is to be noted that the conversion of dinuclear intermediates ( $[\text{Pd}_2\mathbf{1}_2\text{Py}^*_5]^{4+}$  is shown as a typical structure) to the cage (right side) and to the sheet (left side) is not a single step but contains multiple reactions. Without a good template ( $\text{NO}_3^-$ ), an S-shaped conformation of the ditopic ligands **1** is preferred and the energy barrier for the formation of the  $(\text{OTf}^-)@[\text{Pd}_2\mathbf{1}_4]^{4+}$  cage ( $\Delta G_{\text{on}}^\ddagger$ ) is higher than that for the sheet formation ( $\Delta G_{\text{off}}^\ddagger$ ), which biases the self-assembly towards the off-pathway leading to the metastable sheet structure. In the presence of a good template ( $\text{NO}_3^-$ ),  $\Delta G_{\text{on}}^\ddagger$  is smaller than  $\Delta G_{\text{off}}^\ddagger$ , so the self-assembly takes place through the on-pathway to lead to the thermodynamically most stable  $(\text{NO}_3^-)@[\text{Pd}_2\mathbf{1}_4]^{4+}$  cage under kinetic control. If the self-assembly was controlled by the thermodynamic template effect, the product would be determined exclusively by the relative thermodynamic stability between the sheet and the  $(\text{X}^-)@[\text{Pd}_2\mathbf{1}_4]^{4+}$  cage

$[Pd_2I_2]^{4+}$  macrocycle formation in the presence of  $NO_3^-$ . NASAP also supports the strong kinetic template effect on the on-pathway, showing that the rate constants of the intramolecular cyclization in the early stage of the self-assembly ( $k_3$  and  $k_4$ ) are much larger than that in the final step ( $k_5$ ).  $NO_3^-$ , the best template anion, does not only efficiently convert the kinetically trapped sheet structure to the cage but is also able to alter the self-assembly pathway itself by the strong kinetic template effect on the early stage of the self-assembly to take the on-pathway.

## Methods

**General.**  $^1H$  and  $^{19}F$  NMR spectra were recorded using a Bruker AV-500 (500 MHz) spectrometer. All  $^1H$  spectra were referenced using a residual solvent peak,  $CD_3NO_2$  ( $\delta$  4.33).

**Materials.** Unless otherwise noted, all solvents and reagents were obtained from commercial suppliers (TCI Co., Ltd., WAKO Pure Chemical Industries Ltd., KANTO Chemical Co., Inc., and Sigma-Aldrich Co.) and were used as received.  $CD_3NO_2$  was purchased from Acros Organics and used after dehydration with Molecular Sieves 4 Å. Ditopic ligand **1** was prepared according to the literature<sup>35</sup>.

**Monitoring of the self-assembly of the  $(OTf^-)@[Pd_2I_4]^{4+}$  cage.** A 2.4 mM solution of [2.2]paracyclophane in  $CHCl_3$  (125  $\mu$ L), which was used as an internal standard, was added to two NMR tubes (tubes I and II) and the solvent was removed in vacuo. A solution of  $[PdPy^*_4](OTf)_2$  (36 mM) in  $CD_3NO_2$  was prepared (solution A). Solution A (50  $\mu$ L) and  $CD_3NO_2$  (500  $\mu$ L) were added to tube I. The exact concentration of  $[PdPy^*_4](OTf)_2$  in solution A was determined through the comparison of the signal intensity of [2.2]paracyclophane by  $^1H$  NMR. A solution of ditopic ligand **1** (36 mM) in  $CHCl_3$  (100  $\mu$ L) was added to tube II and the solvent was removed in vacuo. Then  $CD_3NO_2$  (550  $\mu$ L) was added to tube II and the exact amount of **1** in tube II was determined through the comparison of the signal intensity with [2.2]paracyclophane by  $^1H$  NMR. 0.50 eq. (against the amount of ligand **1** in tube II) of solution A (ca. 50  $\mu$ L; the exact amount was determined based on the exact concentration of solution A and of ligand in tube II) were added to tube II at 263 K. The self-assembly of the  $(OTf^-)@[Pd_2I_4]^{4+}$  cage was monitored at 298 K by  $^1H$  NMR spectroscopy. An example of the  $^1H$  NMR spectra is shown in Fig. 2 and Supplementary Fig. 1. The exact ratio of **1** and  $[PdPy^*_4](OTf)_2$  was unambiguously determined by the comparison of the integral value of each  $^1H$  NMR signal with those of [2.2]paracyclophane. The amounts of  $[PdPy^*_4]^{2+}$ ,  $[Pd_2I_4]^{4+}$ , and  $Py^*$  were quantified by the integral values of each  $^1H$  NMR signal against the signal of the internal standard ([2.2]paracyclophane). In order to confirm the reproducibility, the same experiment was carried out four times (runs 1–4) in total. These data, the average values of the existence ratios, and the  $\langle n \rangle$ ,  $\langle k \rangle$  values are listed in Supplementary Tables 1–6, 9–11, and 13–17.

**Determination of the existence ratio of each species.** The relative integral value of each  $^1H$  NMR signal against the internal standard [2.2]paracyclophane is used as the integral value in this description. We define the integral values of the signal for the substrates, the products, and the kinetically trapped species at each time  $t$  as follows;  $I_L(t)$ : 1/4 of the integral value of the  $e$  proton in free ligand **1**;  $I_M(t)$ : the integral value of the  $f$  proton of  $Py^*$  in  $[PdPy^*_4]^{2+}$ ;  $I_{cage}(t)$ : 1/4 of the integral value of the  $e$  proton in  $(X^-)@[Pd_2I_4]^{4+}$ ;  $I_{Py^*}(t)$ : the integral value of the  $f$  proton of free  $Py^*$ .

$I_M(0)$  was determined based on the exact concentration of solution A determined by  $^1H$  NMR and the exact volume of solution A added into tube II.  $I_L(0)$  was determined by  $^1H$  NMR measurement before the addition of solution A into tube II.

Existence ratio of  $[PdPy^*_4]^{2+}$ : As the total amount of  $[PdPy^*_4]^{2+}$  corresponds to  $I_M(0)$ , the existence ratio of  $[PdPy^*_4]^{2+}$  at  $t$  is expressed by  $I_M(t)/I_M(0)$ . Existence ratio of **1**: As the total amount of free ligand **1** corresponds to  $I_L(0)$ , the existence ratio of **1** at  $t$  is expressed by  $I_L(t)/I_L(0)$ .

Existence ratio of  $Py^*$ : As the total amount of  $Py^*$  corresponds to  $I_M(0)$ , the existence ratio of  $Py^*$  at  $t$  is expressed by  $I_{Py^*}(t)/I_M(0)$ .

Existence ratio of  $(X^-)@[Pd_2I_4]^{4+}$ : As  $(X^-)@[Pd_2I_4]^{4+}$  is quantified based on **1**, the existence ratio of the cage at  $t$  is expressed by  $I_{cage}(t)/I_L(0)$ .

Existence ratio of the total intermediates not observed by  $^1H$  NMR: The existence ratio of the total intermediates not observed by  $^1H$  NMR is determined based on the amount of ligand **1** in the intermediates. Thus the existence ratio of the total intermediate not observed by  $^1H$  NMR is calculated by subtracting the other species containing **1** (free **1** and  $(X^-)@[Pd_2I_4]^{4+}$ ) from the total amount of **1** ( $I_L(0)$ ). The existence ratio of the total intermediates at  $t$  is expressed by  $(I_L(0) - I_L(t) - I_{cage}(t))$ .

$\langle a \rangle$ : The total amount of Pd(II) ions corresponds to  $I_M(0)/4$ . The amount of Pd(II) ions in  $[PdPy^*_4]^{2+}$  at  $t$  corresponds to  $I_M(t)/4$ . The amount of  $Pd^{2+}$  ions in  $(X^-)@[Pd_2I_4]^{4+}$  at  $t$  corresponds to  $I_{cage}(t)/2$ . The amount of Pd(II) ions in the intermediates at  $t$  is thus expressed by  $I_M(0)/4 - I_M(t)/4 - I_{cage}(t)/2$ .

$\langle b \rangle$ : The total amount of ligand **1** corresponds to  $I_L(0)$ . The amount of free ligand **1** at  $t$  corresponds to  $I_L(t)$ . The amounts of ligand **1** in  $(X^-)@[Pd_2I_4]^{4+}$  at  $t$  corresponds to  $I_{cage}(t)$ . The amount of ligand **1** in the intermediates at  $t$  is thus expressed by  $I_L(0) - I_L(t) - I_{cage}(t)$ .

$\langle c \rangle$ : The total amount of  $Py^*$  corresponds to  $I_M(0)$ . The amount of free  $Py^*$  at  $t$  corresponds to  $I_{Py^*}(t)$ . The amount of  $Py^*$  in  $[PdPy^*_4]^{2+}$  at  $t$  corresponds to  $I_M(t)$ . The amount of  $Py^*$  in the intermediates at  $t$  is thus expressed by  $I_M(0) - I_{Py^*}(t) - I_M(t)$ .

The  $\langle n \rangle$  and  $\langle k \rangle$  values are determined with these  $\langle a \rangle$ ,  $\langle b \rangle$ , and  $\langle c \rangle$  values by Eqs. (1) and (2).

$$\langle n \rangle = \frac{4\langle a \rangle - \langle c \rangle}{\langle b \rangle} \quad (1)$$

$$\langle k \rangle = \frac{\langle a \rangle}{\langle b \rangle} \quad (2)$$

**Quantitative analysis of the self-assembly process.** In QASAP, all the substrates (**1** and  $[PdPy^*_4](OTf)_2$ ), and the products (the  $(X^-)@[Pd_2I_4]^{4+}$  cage and  $Py^*$ ) were quantified by  $^1H$  NMR spectroscopy during the self-assembly and then the amount of the intermediates not observed by  $^1H$  NMR (**Int**) and the average composition of the unobservable intermediates,  $Pd_{(a)}I_{(b)}Py^*_{(c)}$ , were obtained. The existence ratios of the substrates and the products and  $\langle a \rangle$ ,  $\langle b \rangle$ ,  $\langle c \rangle$ ,  $\langle n \rangle$ , and  $\langle k \rangle$  with time are listed in Supplementary Tables 1–6 and 9–17 and plotted in Fig. 3.

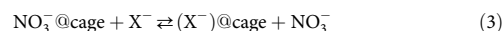
**STEM measurement.**  $[PdPy^*_4](OTf)_2$  (0.595  $\mu$ mol), **1** (1.19  $\mu$ mol), and  $n$ -Bu<sub>4</sub>NOTf (1.19  $\mu$ mol) were quantified and mixed in  $CD_3NO_2$  (ca. 650  $\mu$ L;  $[I]_0 = 1.82$  mM). The solution was left for 4 weeks at 298 K and then diluted 170 times with  $CH_3NO_2$ . Two microliter of the diluted solution was poured onto the substrate (TEM microgrids, Okenshoji Co. Ltd.). Then the substrate was freeze-dried and measurements were carried out. The STEM image is shown in Fig. 4b–e.

**AFM measurement.**  $[PdPy^*_4](OTf)_2$  (0.595  $\mu$ mol), **1** (1.19  $\mu$ mol), and  $n$ -Bu<sub>4</sub>NOTf (1.19  $\mu$ mol) were quantified and mixed in  $CD_3NO_2$  (ca. 650  $\mu$ L;  $[I]_0 = 1.82$  mM). The solution was left for 4 weeks at 298 K and then diluted 170 times with  $CH_3NO_2$ . Ten microliter of the diluted solution was poured onto the substrate (graphene). Then the substrate was freeze-dried and vacuumed overnight. The AFM image is shown in Fig. 4f–i.

**Anion competition experiments.**  $^{19}F$  DOSY NMR measurements confirm the encapsulation of  $OTf^-$  in the cavity of the  $[Pd_2I_4]^{4+}$  cage. Anion competition experiments have been carried out by adding 4 eq. to cage (1 eq. to the anion already present in solution) of tetrabutylammonium ( $n$ -Bu<sub>4</sub>N) salts of various polyatomic anions. Displacement of the encapsulated anions has been observed through  $^1H$  and  $^{19}F$  NMR measurements (Supplementary Figs. 7–9).

One hundred microliter of a 3 mM  $CD_3NO_2$  solution of the cage (0.3  $\mu$ mol) was added to an NMR tube. Four hundred microliter of  $CD_3NO_2$  were then added. At this stage, the cage is encapsulating  $OTf^-$ , and the addition of a different anion will determine the relative binding strengths to the cage of the two anions. Fifty microliter of a 24 mM solution of the tetrabutylammonium salts of the anion of interest (1.2  $\mu$ mol) was added to the NMR tube and the encapsulation process was monitored by  $^{19}F$  NMR spectroscopy. Next, 50  $\mu$ L of a 24 mM solution of a different anion were added to the solution. The solutions of the cage and anions were prepared beforehand based on the following molecular weights: cage 1865.5 g mol<sup>-1</sup>;  $n$ -Bu<sub>4</sub>NPF<sub>6</sub> 387.43 g mol<sup>-1</sup>;  $n$ -Bu<sub>4</sub>NBF<sub>4</sub> 329.27 g mol<sup>-1</sup>;  $n$ -Bu<sub>4</sub>NClO<sub>4</sub> 341.91 g mol<sup>-1</sup>.

**Determination of the relative binding affinities of anions.** In order to quantitatively determine the relative affinities of the different anions to the  $[Pd_2I_4]^{4+}$  cage, anion competition experiments starting from the cage encapsulating the strongest bound anion ( $NO_3^-$ ) were performed (Eq. (3)).



A 2.4 mM solution of [2.2]paracyclophane in  $CHCl_3$  (125  $\mu$ L), which was used as an internal standard, was added to an NMR tube and the solvent was removed in vacuo. Two hundred microliter of a 0.5 mM solution of  $(NO_3^-)@[Pd_2I_4]^{4+}$  in  $CD_3NO_2$  were added to the NMR tube, followed by 300  $\mu$ L of  $CD_3NO_2$ . The exact concentration of  $(NO_3^-)@[Pd_2I_4]^{4+}$  in the solution was determined through the comparison of the signal intensity of [2.2]paracyclophane by  $^1H$  NMR spectroscopy. Solutions of  $n$ -Bu<sub>4</sub>NX ( $X = ClO_4$ ,  $BF_4$ ,  $PF_6$ , and  $OTf$ ) with concentrations varying based on their binding strength ( $n$ -Bu<sub>4</sub>NClO<sub>4</sub>: 40 mM,  $n$ -Bu<sub>4</sub>NBF<sub>4</sub>: 200 mM,  $n$ -Bu<sub>4</sub>NPF<sub>6</sub>: 400 mM,  $n$ -Bu<sub>4</sub>NOTf: 400 mM) were prepared in  $CD_3NO_2$ . Increasing amounts (from 10 to 100  $\mu$ L) of an anion solution was added and  $^1H$  NMR spectra were recorded. The amount of  $n$ -Bu<sub>4</sub>NX added was controlled in order to obtain  $(NO_3^-)@[Pd_2I_4]^{4+}$  and the new cage encapsulating a different anion in equilibrium, to enable quantification. The relative binding constants

( $K_{\text{comp}}$ ) was defined by Eq. (4).

$$K_{\text{comp}} = \frac{[(X^-)@cage][NO_3^-]}{[NO_3^-@cage][X^-]} \quad (4)$$

As the total concentration of  $NO_3^-$  is four times the initial concentration of the cage before the addition of  $n\text{-Bu}_4NX$  ( $[(NO_3^-)@cage]_0$ ,  $[NO_3^-]$  can be expressed by Eq. (5).

$$[NO_3^-] = 4 \times [(NO_3^-)@cage]_0 - [(NO_3^-)@cage] \quad (5)$$

$[X^-]$  in Eq. (4) is expressed by Eq. (6)

$$[X^-] = [n\text{-Bu}_4N^+] - [(X^-)@cage] \quad (6)$$

Thus, using Eqs. (5) and (6), Eq. (4) is expressed by Eq. (7).

$$K_{\text{comp}} = \frac{[(X^-)@cage] \cdot (4 \cdot [(NO_3^-)@cage] - [(NO_3^-)@cage])}{[NO_3^-@cage] \cdot ([n\text{-Bu}_4N^+] - [(X^-)@cage])} \quad (7)$$

As all the concentrations in Eq. (7) can be determined by  $^1H$  NMR spectroscopy,  $K_{\text{comp}}$  were calculated using Eq. (7). The data used for the calculation of the  $K_{\text{comp}}$  values for  $X = ClO_4$ ,  $BF_4$ , and  $PF_6$  are summarized in Supplementary Table 8. The  $K_{\text{comp}}$  values for  $OTf^-$  were not determined as the binding strength difference between this anion and  $NO_3^-$  was too large, and no peaks for  $(OTf^-)@[Pd_2I_4]^{4+}$  were observed even after the addition of 1200 eq. of  $n\text{-Bu}_4NOTf$  to  $(NO_3^-)@[Pd_2I_4]^{4+}$ .

**Competition experiment for  $NO_3^-$  between the cage and the macrocycle.** The  $(NO_3^-)@[Pd_2I_4]^{4+}$  macrocycle was prepared from  $[PdPy_2](OTf)_2$  and **1** in the presence of  $n\text{-Bu}_4NNO_3$  in  $CD_3NO_2$  at 298 K. To this solution, a solution of 1 eq. of  $(OTf^-)@[Pd_2I_4](OTf)_3$  in  $CD_3NO_2$  was added.  $^1H$  NMR spectra shown in Supplementary Fig. 21 show peaks corresponding to  $(NO_3^-)@[Pd_2I_4]^{4+}$  and  $[Pd_2I_4]^{4+}$ , indicating that the  $NO_3^-$  anion initially bound to the  $[Pd_2I_4]^{4+}$  macrocycle was selectively encapsulated by the  $[Pd_2I_4]^{4+}$  cage, demonstrating the stronger affinity of  $NO_3^-$  for the cage rather than for the macrocycle.

**X-ray analysis of  $(NO_3^-)@[Pd_2I_4]^{4+}$ .** The single crystal was immersed in and coated with Paratone N oil (Hampton Research Corp.), and mounted on a MicroMount™ (MiteGen LLC). Diffraction data of the single crystal were collected on a SuperNova single-crystal X-ray diffractometer with an Eos CCD detector (Rigaku Oxford Diffraction) at 294 K under ambient conditions, using Cu K $\alpha$  ( $\lambda = 1.54184$  Å) radiation monochromated by multilayer mirror optics. Bragg spots were integrated using the CrysAlisPro program package (Rigaku Oxford Diffraction). An empirical absorption correction based on the multi-scan method using spherical harmonics was implemented in the SCALE3 ABSPACK scaling algorithm. The structure was solved by an intrinsic phasing method on the SHELXT program<sup>52</sup> and refined by a full-matrix least-squares minimization on  $F^2$  executed by the SHELXL program<sup>53</sup>, using the Olex2 software package (OlexSys Ltd)<sup>54</sup>. The structure was determined as an inversion twin having the polar space group of  $Aea2$  by using a twin law matrix:  $-1\ 0\ 0\ 0\ 1\ 0\ 0\ 0\ -1$ , where the Flack parameter<sup>55</sup> was given as 0.004(3). Thermal displacement parameters were refined anisotropically for all non-hydrogen atoms. All the hydrogen atoms were located at calculated positions and the parameters were refined with a riding model. For counter anions, we could find a disordered  $NO_3^-$  molecule in the  $[Pd_2I_4]^{4+}$  cage and two  $OTf^-$  molecules, which are crystallographically equivalent to each other, in the clearance of the crystal. However, another anion could not be satisfactorily solved due to a terrible disorder. The data were corrected for disordered electron density by using the PLATON SQUEEZE method<sup>56</sup>. The crystal structure is shown in Fig. 5 and Supplementary Figs. 18 and 19. Crystallographic data and structural characteristics of the cage are summarized in Supplementary Tables 18 and 19, respectively. Crystallographic information file for  $(NO_3^-)@[Pd_2I_4]^{4+}$  is provided in Supplementary Data 1. The X-ray crystallographic coordinates for structures reported in this Article have been deposited at the Cambridge Crystallographic Data Centre (CCDC), under deposition number CCDC 1935011. These data can be obtained free of charge from the CCDC via [http://www.ccdc.cam.ac.uk/data\\_request/cif](http://www.ccdc.cam.ac.uk/data_request/cif).

**Numerical analysis of self-assembly process of the cage.** For the numerical analysis of self-assembly process (NASAP), a reaction network for the self-assembly of the  $[Pd_2I_4]^{4+}$  cage, which is indicated as (2,4,0), is constructed as follows. Starting from the final cage (2,4,0), the reaction path is traced back to the substrates, that is,  $[PdPy_4]^{2+}$  and **1**. In this back propagation process, all the directly accessible molecular species are considered as the intermediates. Note that in this network model the intermediate species consisting of more components than the cage (2,4,0) are excluded. With this procedure taken, it is found that the total of 29 molecular species (including both the reactants and the products themselves) construct a minimal reaction network composed of 68 reactions, each of which contain the forward and backward processes. The resultant minimal reaction network is shown in Supplementary Fig. 22.

Although we call it minimal, this reaction network turns out to be so large that it is impossible to assign rate constants to each reaction and to search for the parameters in such a vast parameter space to fit the experimental results best.

Therefore, we divided the whole network into five classes possessing similar characteristics and defined the rate constants in Fig. 7a:

Type I: For the coordination of a free ditopic ligand **1** releasing a leaving ligand  $Py^*$ :  $k_1$  [ $\text{min}^{-1} \text{M}^{-1}$ ] and  $k_{-1}$  [ $\text{min}^{-1} \text{M}^{-1}$ ] for the forward and backward reactions, respectively.

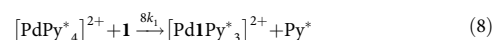
Type II: For the formation of dinuclear species from two mononuclear species, with  $Pd(II)$  ions bridged by a ditopic ligand **1**:  $k_2$  [ $\text{min}^{-1} \text{M}^{-1}$ ] and  $k_{-2}$  [ $\text{min}^{-1} \text{M}^{-1}$ ] for the forward and backward reactions, respectively.

Type III: For the cyclization in dinuclear species:  $k_3$  [ $\text{min}^{-1}$ ] and  $k_{-3}$  [ $\text{min}^{-1} \text{M}^{-1}$ ] for the forward and backward reactions, respectively.

Type IV: For the cross-linking in dinuclear species:  $k_4$  [ $\text{min}^{-1}$ ] and  $k_{-4}$  [ $\text{min}^{-1} \text{M}^{-1}$ ] for the forward and backward reactions, respectively.

Type V: For the final reaction (cage completion):  $k_5$  [ $\text{min}^{-1}$ ] and  $k_{-5}$  [ $\text{min}^{-1} \text{M}^{-1}$ ] for the forward and backward reaction, respectively.

Note here that each rate constant is defined per reaction site, based on the modeling procedure reported previously. So the actual reaction rate for each reaction is estimated as the above constant multiplied by the total number of available combinations. For example, for a ligand reaction between  $[PdPy_4]^{2+}$  and **1** to produce  $[PdI_2Py_3]^{2+}$  and  $Py^*$ , the rate constant is given as  $k_1$  times 4 (the number of  $Pd-Py^*$  bonds in  $[PdPy_4]^{2+}$ ) times 2 (the number of coordination sites in **1**), i.e.,



We adopted this setting to explicitly distinguish the structural difference among the species with the same composition.

In order to numerically track the time evolution of the existence ratios for both reactants and products and the  $\langle n \rangle$ ,  $\langle k \rangle$  values, we have adopted a stochastic approach based on the chemical master equation, the so-called Gillespie algorithm<sup>57–60</sup>. In this algorithm, for all the possible  $N$  reactions including molecular species  $S_{ai}$ ,  $S_{bi}$ ,  $S_{ci}$ , ...

$$S_{ai} + S_{bi} + \dots \rightarrow S_{ci} + \dots \quad (i = 1, \dots, N) \quad (9)$$

The total reaction rate  $R_{\text{tot}}$  is calculated as

$$R_{\text{tot}} = r_1 + r_2 + \dots + r_N \quad (10)$$

$$r_i = k_i[S_{ai}][S_{bi}] \dots$$

Starting from the initial time  $t = 0$ , at each instant  $t$ , which one of the reactions to occur is determined with the uniform random number,  $s_1 \in (0, 1)$  as

$$\begin{aligned} &\text{if } s_1 \leq \frac{r_1}{R_{\text{tot}}}, \text{ then reaction 1 occurs,} \\ &\text{if } \frac{r_1}{R_{\text{tot}}} < s_1 \leq \frac{r_1+r_2}{R_{\text{tot}}}, \text{ then reaction 2 occurs,} \\ &\text{if } \frac{r_1+\dots+r_{N-1}}{R_{\text{tot}}} < s_1 \leq 1, \text{ then reaction } N \text{ occurs.} \end{aligned}$$

Another uniform random number  $s_2 \in (0, 1)$  is independently given to fix the incremental  $dt$  as

$$dt = \ln(1/s_2)/R_{\text{tot}} \quad (11)$$

Time is updated as  $t = t + dt$ , together with the update of the numbers of corresponding molecular species, i.e.,  $S_{ai} \rightarrow S_{ai} - 1$ ,  $S_{bi} \rightarrow S_{bi} - 1$ ,  $S_{ci} \rightarrow S_{ci} + 1$ , ... The reason why this approach traces the chemical reactions and actually works well is given in the literatures in detail, along with the practical way to implement it<sup>57–60</sup>.

With the initial conditions (numbers of species),  $\langle PdPy_4 \rangle_0 = 1,200$ ,  $\langle \mathbf{1} \rangle_0 = 2,400$ ,  $\langle \text{others} \rangle_0 = 0$ , rate constant search was performed in a ten-dimensional parameter space ( $k_1, k_{-1}, k_2, k_{-2}, k_3, k_{-3}, k_4, k_{-4}, k_5, k_{-5}$ ). The Avogadro number and the volume of the simulation box were set to be  $N_A = 6.0 \times 10^{23}$  and  $V = 2.0 \times 10^{-18}$  L, respectively, which gives the same concentrations as the experiments were carried out under. After the rate constant search was finished, refined simulations were performed for some rate parameter sets that give existence ratios and  $\langle n \rangle$ ,  $\langle k \rangle$  plot in good agreement with the experimental counterparts. The adequacy of the fitting to the experimental data was evaluated from the residual sum of squares (RSS) with the average of the experimental data, obtained from three runs. For all the time steps  $t_i$  at which the experimental data of existence ratios  $R_{\text{ex}}^S$  and parameters  $n_{\text{ex}}$  and  $k_{\text{ex}}$  are available, RSS's are calculated with the numerically obtained values  $R_{\text{nu}}^S$  and so on as (note that  $S = [PdPy_4]^{2+}$ , **1**,  $[Pd_2I_4]^{4+}$ , or  $Py^*$ ),

$$RSS_1 = \sum_{t_i} \sum_S \left( R_{\text{nu},t_i}^S - R_{\text{ex},t_i}^S \right)^2 \quad (12)$$

$$RSS_2 = \sum_{t_i} \left( n_{\text{nu},t_i} - n_{\text{ex},t_i} \right)^2 + \sum_{t_i} \left( k_{\text{nu},t_i} - k_{\text{ex},t_i} \right)^2 \quad (13)$$

A representative result is shown in Fig. 7b–d, in which the initial particles and the volume of the simulation box were set to be a hundred times larger than the rough parameter search, i.e.,  $\langle PdPy_4 \rangle_0 = 120,000$ ,  $\langle \mathbf{1} \rangle_0 = 240,000$ , and  $V = 2.5 \times 10^{-16}$  L. A similar behavior was confirmed with several runs for the particle numbers given above.

## Data availability

The authors declare that all the other data supporting the findings of this study are available within the article and its supplementary information files and from the

corresponding author upon request. Crystallographic information file for  $(\text{NO}_3^-)_4@[\text{Pd}_2\text{L}_4]^{2+}$  is provided in Supplementary Data 1. The X-ray crystallographic coordinates for structures reported in this Article have been deposited at the CCDC, under deposition number CCDC 1935011. These data can be obtained free of charge from the CCDC via [http://www.ccdc.cam.ac.uk/data\\_request/cif](http://www.ccdc.cam.ac.uk/data_request/cif).

Received: 2 August 2019; Accepted: 23 October 2019;

Published online: 13 November 2019

## References

- Thompson, M. C. & Busch, D. H. Reactions of coordinated ligands. VI. metal ion control in the synthesis of planar nickel(II) complexes of  $\alpha$ -diketo-bis-mercaptoimines. *J. Am. Chem. Soc.* **86**, 213–217 (1964).
- Anderson, S., Anderson, H. L. & Sanders, J. K. M. Expanding roles for templates in synthesis. *Acc. Chem. Res.* **26**, 469–475 (1993).
- Greene, R. N. 18-crown-6: a strong complexing agent for alkali metal cations. *Tetrahedron Lett.* **13**, 1793–1796 (1972).
- Kulstad, S. & Malmsten, L.  $\ddot{\text{A}}$ . Diaza-crown ethers – VI: a mechanism for metal ion promoted formation of macrocyclic diazaoligoethers. *Tetrahedron* **36**, 521–523 (1980).
- Anderson, H. L. & Sanders, J. K. M. Amine-template-directed synthesis of cyclic porphyrin oligomers. *Angew. Chem. Int. Ed. Engl.* **29**, 1400–1403 (1990).
- Gerbelet, N. V., Arion, V. B. & Burgess, J. P. *Template Synthesis of Macrocyclic Compounds*. (WILEY-VCH, Weinheim, 1999).
- Hubin, T. J. & Busch, D. H. Template routes to interlocked molecular structures and orderly molecular entanglements. *Coord. Chem. Rev.* **200** – 202, 5–52 (2000).
- Martí-Centelles, V., Burguete, M. I. & Luis, S. V. Template effects in  $\text{S}_{\text{N}}2$  displacements for the preparation of pseudopeptidic macrocycles. *Chem. Eur. J.* **18**, 2409–2422 (2012).
- Liu, S. et al. Caterpillar track complexes in template-directed synthesis and correlated molecular motion. *Angew. Chem. Int. Ed.* **54**, 5355–5359 (2015).
- Makeiff, D. A., Pope, D. J. & Sherman, J. C. Template effects in the formation of a tetramethylene-bridged hemicarceplex. *J. Am. Chem. Soc.* **122**, 1337–1342 (2000).
- Moure, A., Luis, S. V. & Alfonso, I. Efficient synthesis of pseudopeptidic molecular cages. *Chem. Eur. J.* **18**, 5496–5500 (2012).
- Dietrich-Buchecker, C. O., Sauvage, J.-P. & Kintzinger, J. P. Une nouvelle famille de molécules: les metallo-catenanes. *Tetrahedron Lett.* **24**, 5095–5098 (1983).
- Yang, X., Knobler, C. B. & Hawthorne, M. F. “[12]Mercuracarborand-4”, the first representative of a new class of rigid macrocyclic electrophiles: the chloride ion complex of a charge-reversed analogue of [12]crown-4. *Angew. Chem. Int. Ed. Engl.* **30**, 1507–1508 (1991).
- Amabilino, D. B. & Stoddart, J. F. Interlocked and intertwined structures and superstructures. *Chem. Rev.* **95**, 2725–2828 (1995).
- Hasenknopf, B., Lehn, J.-M., Kneisel, B. O., Baum, G. & Fenske, D. Self-assembly of a circular double helicate. *Angew. Chem. Int. Ed. Engl.* **35**, 1838–1840 (1996).
- Dietrich-Buchecker, C., Rapenne, G. & Sauvage, J.-P. Efficient synthesis of a molecular knot by copper(I)-induced formation of the precursor followed by ruthenium(II)-catalysed ring closing metathesis. *Chem. Commun.* 2053–2054 (1997).
- Hübner, G. M., Gläser, J., Seel, C. & Vögtle, F. High-yielding rotaxane synthesis with an anion template. *Angew. Chem. Int. Ed.* **38**, 383–386 (1999).
- Adams, H. et al. Knot tied around an octahedral metal centre. *Nature* **411**, 763–763 (2001).
- Ghosh, P., Mermagen, O. & Schalley, C. A. Novel template effect for the preparation of [2]rotaxanes with functionalised centre pieces. *Chem. Commun.* 2628–2629 (2002).
- Wisner, J. A., Sambrook, M., Drew, M. G. B. & Beer, P. D. Anion-templated rotaxane formation. *J. Am. Chem. Soc.* **124**, 12469–12476 (2002).
- Chichak, K. S. et al. Molecular Borromean Rings. *Science* **304**, 1308–1312 (2004).
- Vickers, M. S. & Beer, P. D. Anion templated assembly of mechanically interlocked structures. *Chem. Soc. Rev.* **36**, 211–225 (2007).
- Crowley, J. D., Goldup, S. M., Lee, A.-L., Leigh, D. A. & McBurney, R. T. Active metal template synthesis of rotaxanes, catenanes and molecular shuttles. *Chem. Soc. Rev.* **38**, 1530–1541 (2009).
- Beves, J. E., Blight, B. A., Campbell, C. J., Leigh, D. A. & McBurney, R. T. Strategies and tactics for the metal-directed synthesis of rotaxanes, knots, catenanes, and higher order links. *Angew. Chem. Int. Ed.* **50**, 9260–9327 (2011).
- Forgan, R. S., Sauvage, J.-P. & Stoddart, J. F. Chemical topology: complex molecular knots, links, and entanglements. *Chem. Rev.* **111**, 5434–5464 (2011).
- Arias, K. I., Zysman-Colman, E., Loren, J. C., Linden, A. & Siegel, J. S. Synthesis of a  $D_3$ -symmetric “trefoil” knotted cyclophane. *Chem. Commun.* **47**, 9588–9590 (2011).
- Denis, M. & Goldup, S. M. The active template approach to interlocked molecules. *Nat. Rev. Chem.* **1**, 0061 (2017).
- Gies, H. & Marler, B. The structure-controlling role of organic templates for the synthesis of porosils in the systems  $\text{SiO}_2/\text{template}/\text{H}_2\text{O}$ . *Zeolites* **12**, 42–49 (1992).
- Zelenski, C. M. & Dorhout, P. K. Template synthesis of near-monodisperse microscale nanofibers and nanotubules of  $\text{MoS}_2$ . *J. Am. Chem. Soc.* **120**, 734–742 (1998).
- Hernandez, B. A., Chang, K.-S., Fisher, E. R. & Dorhout, P. K. Sol-gel template synthesis and characterization of  $\text{BaTiO}_3$  and  $\text{PbTiO}_3$  nanotubes. *Chem. Mater.* **14**, 480–482 (2002).
- Hou, S., Harrell, C. C., Trofin, L., Kohli, P. & Martin, C. R. Layer-by-layer nanotube template synthesis. *J. Am. Chem. Soc.* **126**, 5674–5675 (2004).
- Xu, H. & Wang, W. Template synthesis of multishelled  $\text{Cu}_2\text{O}$  hollow spheres with a single-crystalline shell wall. *Angew. Chem. Int. Ed.* **46**, 1489–1492 (2007).
- Liang, H.-W. et al. Macroscopic-scale template synthesis of robust carbonaceous nanofiber hydrogels and aerogels and their applications. *Angew. Chem. Int. Ed.* **51**, 5101–5105 (2012).
- Liu, J. et al. A facile soft-template synthesis of mesoporous polymeric and carbonaceous nanospheres. *Nat. Commun.* **4**, 2798 (2013).
- McMorran, D. A. & Steel, P. J. The first coordinatively saturated, quadruply stranded helicate and its encapsulation of a hexafluorophosphate anion. *Angew. Chem. Int. Ed.* **37**, 3295–3297 (1998).
- Steel, P. J. & McMorran, D. A. Selective anion recognition by a dynamic quadruple helicate. *Chem. Asian J.* **14**, 1098–1101 (2019).
- Tsujimoto, Y., Kojima, T. & Hiraoka, S. Rate-determining step in the self-assembly process of supramolecular coordination capsules. *Chem. Sci.* **5**, 4167–4172 (2014).
- Hiraoka, S. Unresolved issues that remain in molecular self-assembly. *Bull. Chem. Soc. Jpn.* **91**, 957–978 (2018).
- Hiraoka, S. Self-assembly processes of Pd(II)- and Pt(II)-linked discrete self-assemblies revealed by QASAP. *Isr. J. Chem.* **59**, 151–165 (2019).
- Kai, S. et al. Flexibility of components alters the self-assembly pathway of  $\text{Pd}_2\text{L}_4$  coordination cages. *Dalton Trans.* **47**, 3258–3263 (2018).
- Desiraju, G. R. The C–H...O hydrogen bond in crystals: what is it? *Acc. Chem. Res.* **24**, 290–296 (1991).
- Desiraju, G. R. The C–H...O hydrogen bond: structural implications and supramolecular design. *Acc. Chem. Res.* **29**, 441–449 (1996).
- Jiang, L. & Lai, L. CH...O hydrogen bonds at protein-protein interfaces. *J. Bio. Chem.* **277**, 37732–37740 (2002).
- Scheiner, S. & Kar, T. Spectroscopic and structural signature of the CH–O hydrogen bond. *J. Phys. Chem. A* **112**, 11854–11860 (2008).
- Zhou, L.-P. & Sun, Q.-F. A self-assembled  $\text{Pd}_2\text{L}_4$  cage that selectively encapsulates nitrate. *Chem. Commun.* **51**, 16767–16770 (2015).
- Kai, S. et al. Quantitative analysis of self-assembly process of a  $\text{Pd}_2\text{L}_4$  cage consisting of rigid ditopic ligands. *Chem. Eur. J.* **24**, 663–671 (2018).
- Basolo, F. & Pearson, R. G. *Mechanisms of inorganic reactions*. (Wiley, New York, 1967).
- Canoves, L., Cattalini, L., Uguagliati, P. & Tobe, M. L. The appearance of a stable intermediate in some substitution reactions of (1,5-diamino-3-azapentene)pyridinepalladium(II) perchlorate. *J. Chem. Soc. Dalton Trans.* 867–872 (1990).
- Matsumura, Y., Hiraoka, S. & Sato, H. A reaction model on the self-assembly process of octahedron-shaped coordination capsules. *Phys. Chem. Chem. Phys.* **19**, 20338–20342 (2017).
- Takahashi, S., Sasaki, Y., Hiraoka, S. & Sato, H. A stochastic model study on the self-assembly process of a  $\text{Pd}_2\text{L}_4$  cage consisting of rigid ditopic ligands. *Phys. Chem. Chem. Phys.* **21**, 6341–6347 (2019).
- Komine, S., Takahashi, S., Kojima, T., Sato, H. & Hiraoka, S. Self-assembly processes of octahedron-shaped  $\text{Pd}_6\text{L}_4$  cages. *J. Am. Chem. Soc.* **141**, 3178–3186 (2019).
- Sheldrick, G. M. *SHELXT* - Integrated space-group and crystal-structure determination. *Acta Crystallogr. Sect. A* **71**, 3–8 (2015).
- Sheldrick, G. M. Crystal structure refinement with *SHELXL*. *Acta Crystallogr. Sect. C* **71**, 3–8 (2015).
- Dolomanov, O. V., Bourhis, L. J., Gildea, R. J., Howard, J. A. K. & Puschmann, H. *OLEX2*: a complete structure solution, refinement and analysis program. *J. Appl. Crystallogr.* **42**, 339–341 (2009).
- Flack, H. D. & Bernardinelli, G. Absolute structure and absolute configuration. *Acta Crystallogr. Sect. A* **55**, 908–915 (1999).
- Spek, A. L. Structure validation in chemical crystallography. *Acta Crystallogr. Sect. D* **65**, 148–155 (2009).

57. Gillespie, D. T. A general method for numerically simulating the stochastic time evolution of coupled chemical reactions. *J. Comput. Phys.* **22**, 403–434 (1976).
58. Gillespie, D. T. Exact stochastic simulation of coupled chemical reactions. *J. Phys. Chem.* **81**, 2340–2361 (1977).
59. Gillespie, D. T. A rigorous derivation of the chemical master equation. *Phys. A* **188**, 404–425 (1992).
60. Gillespie, D. T. Stochastic simulation of chemical kinetics. *Annu. Rev. Phys. Chem.* **58**, 35–55 (2007).

### Acknowledgements

This work was supported by JSPS KAKENHI Grant Numbers 19H02731, 19K22196, 19K15531, 19H05459, and 19H04563 and The Asahi Glass Foundation.

### Author contributions

L.H.F.-T., T.T., W.Z., T.K., and S.H. conceived the project. S.H. prepared the manuscript and all the authors discussed the results and commented on the manuscript. L.H.F.-T. and W.Z. carried out QASAP. L.H.F.-T. carried out competition experiments and self-assembly of the Pd(II) complexes under various conditions. T.T., R.S. K.H., and E.N. performed STEM measurements. T.T. performed AFM measurements. L.H.F.-T. and A.O. carried out single-crystal X-ray measurement and analysis. S.T. and H.S. carried out NASAP.

### Competing interests

The authors declare no competing interests.

### Additional information

**Supplementary information** is available for this paper at <https://doi.org/10.1038/s42004-019-0232-2>.

**Correspondence** and requests for materials should be addressed to S.H.

**Reprints and permission information** is available at <http://www.nature.com/reprints>

**Publisher's note** Springer Nature remains neutral with regard to jurisdictional claims in published maps and institutional affiliations.



**Open Access** This article is licensed under a Creative Commons Attribution 4.0 International License, which permits use, sharing, adaptation, distribution and reproduction in any medium or format, as long as you give appropriate credit to the original author(s) and the source, provide a link to the Creative Commons license, and indicate if changes were made. The images or other third party material in this article are included in the article's Creative Commons license, unless indicated otherwise in a credit line to the material. If material is not included in the article's Creative Commons license and your intended use is not permitted by statutory regulation or exceeds the permitted use, you will need to obtain permission directly from the copyright holder. To view a copy of this license, visit <http://creativecommons.org/licenses/by/4.0/>.

© The Author(s) 2019